# Systematic Analysis of the Impact of Bump Height Manufacturing Errors on the Unbalance Response of a Foil Journal Bearing

Omar Benchekroun, Mihaï Arghir

## To cite this version:

Omar Benchekroun, Mihaï Arghir. Systematic Analysis of the Impact of Bump Height Manufacturing Errors on the Unbalance Response of a Foil Journal Bearing. Journal of Vibration and Acoustics, 2021, 143 (1), pp.011012. ⟨10.1115/1.4047864⟩. ⟨hal-05009252⟩

HAL Id: hal-05009252
https://hal.science/hal-05009252v1

Submitted on 27 Mar 2025

# Systematic analysis of the impact of bump height manufacturing errors on the unbalance response of a foil journal bearing

Omar Benchekroun[1], Mihai Aghir[2]

[1]LTDS, UMR CNRS 5513, University of Lyon, Ecole Centrale de Lyon, ENISE, ENTPE, 69130, Ecully, France, omar.benchekroun@ec-lyon.fr

[2]Institut PRIME, UPR CNRS 3346, Université de Poitiers, ISAE ENSMA, 86962, Futuroscope Chasseneuil, France, mihai.arghir@univ-poitiers.fr

***Abstract***

The present work presents the numerical investigation of the bump height manufacturing errors on the unbalance response of an aerodynamic foil journal bearing. This is the first study of the impact of manufacturing errors based on an important number of samples. A statistical analysis predicts the mean values of the characteristics and the standard errors of the mean. The paper presents the most important aspects of the numerical model that was used and the way it was implemented for the unbalance analysis of a four degrees of freedom rotor. It was considered that the bump height manufacturing errors had a normal distribution (i.e. each bump had a different random height) around the design (mean) height value. The standard deviation of the bump heights (the same for all bumps) is a measure of the magnitude of the manufacturing errors. The results give a qualitative but above all quantitative overview of the impact of machining errors on some characteristics of aerodynamic foil bearings.

**Keywords**: aerodynamic foil bearing, manufacturing errors, rotordynamics

## 1. Introduction

Aerodynamic foil journal bearings represent one of the technologies under meticulous examination when designing high speed rotating machinery. These bearings are used because they bring the much required damping [1] and they do not require a specific lubricant [2] (they can operate with the process gas). Their damping characteristics are due to the compliant structure of their bearing that is made of very thin metallic foils. Many types of foil bearings were developed, but the bump type bearing depicted in Figure 1 is the most popular [3]. It consists of two metallic foils. The top foil is smooth and collects the thin gas film pressures created by the high speed rotating journal. The second sheet is composed of a set of bumps that act like springs. The radial deformation created by the pressure forces produces also a circumferential (tangential) deformation of the bump. All the bumps acts as interconnected springs. The two sheets are welded to the housing at one end and free at the other end. There are many kinds of the bump type foil bearings depending on the number of top and bump foils and on their organization in the axial and circumferential direction. [3].

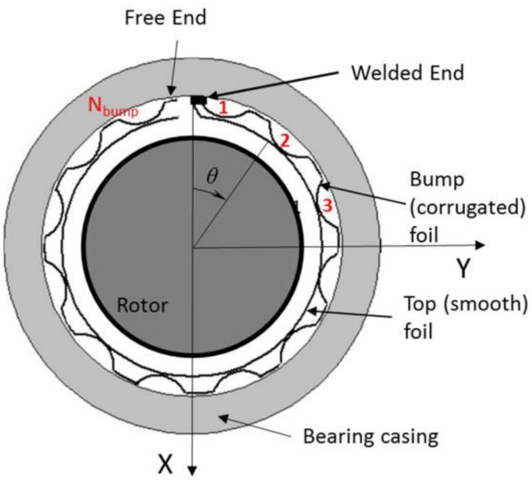

*Figure 1 Bump type foil bearing of first generation*

However, the development and the industrial use of these bearings is not as extensive as it was expected one or two decades ago. One of the reasons could be the absence of a generally accepted theoretical model for predicting their characteristics. For comparison, design procedures of non-complying bearings lubricated with oil or air exist since long [4]. Another possible reason that delays their widespread use is the complicated manufacturing process and the manufacturing tolerances that may result. The manufacturing process was first detailed in [5] and was subsequently used, modified or improved. The foils are of a special alloy with a high yield stress that conserves its modulus of elasticity at high temperatures. The foils are submitted to successive heat treatments and plastic deformations that may induce manufacturing errors [6].

It is realistically considered that manufacturing errors of the bump foil prevail compared to the errors of the top foil. Three realistic manufacturing errors, namely the bump height, the bump length, and the radius of the bump foil were investigated in [7]. Each of these parameters was considered to follow a normal distribution with a mean (design) value and a standard deviation. The standard deviation was 5% or 10% of the design value. Each bump carried a different error. The foil structure was modeled using a commercial code for non-linear elasticity taking into account closed/loose contacts and friction forces. The static stiffness of the foil structure was investigated by considering a rotor radial displacement larger than the clearance. The results showed that only the manufacturing errors of the bump height depicted in Figure 2 affect the stiffness of the foil structure. The analysis was continued in [8] where the unbalance response of a Jeffcottt rotor supported on foil bearings carrying the same bump height manufacturing errors was analyzed.

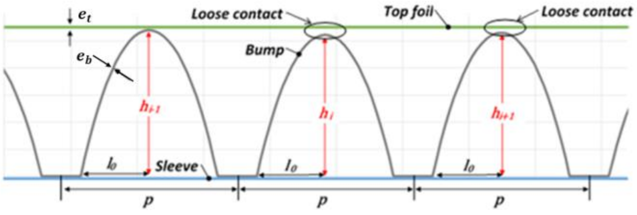

*Figure 2: Description of bump foil errors.*

The analyses published in [7] and [8] were however limited because they presented only a few examples of the impact of manufacturing errors on the characteristics of the foil bearings. A quantitative evaluation of the influence of the manufacturing errors would have required a large number of calculations and a statistical interpretation of the results. This was not possible because the calculation time for the full 3D non-linear analysis was prohibitive.

This remark opens the question of the theoretical model appropriate for such analyses, i.e. accurate enough for taking into account all design details but efficient for performing a large number of calculations. The Reynolds equation for the compressible film of the journal bearing raises no question but the structural model of the foil structure is still a subject of discussions.

**Models of the compliant structure**

The simplest theoretical models consider the compliant structure as a one-dimensional Winkler foundation of infinite axial length ([9] - [12]). Each bump is discretized as an independent spring. These models are easy to implement and require reduced computational resources. Their main weakness is the independence of bumps. Indeed, the bumps are part of the same foil and they interact: the displacement of a bump is linked to the displacement of the neighbor bumps and hence all the bumps are coupled. Moreover, the contacts between the bumps and the top foil or between the bumps and the housing may become loose and the friction forces may restrict the displacements through stick-slip effects. Another weakness is the fact that these simplified models cannot reproduce the damping produced by structural friction forces. This effect must be introduced via an ad-hoc factor. These critics show that a model of this kind would not be credible for estimating the impact of manufacturing errors on the characteristics of the bearing.

At the opposite side are three-dimensional, non-linear elasticity models of the foil structure as previously cited. They are generally based on commercial codes [7], [8], [13] or [14] and have met some success with experienced users. Simplifying assumptions are not needed. These approaches consider the three-dimensional foil structure with gaps and non-linear friction forces, large displacements and material nonlinearities. The analysis of the manufacturing errors cited above was carried out with such a model, but as indicated, an intensive calculation was not possible due to the high calculation effort required especially by dynamic calculations.

An intermediate class of models are based on a compromise between the simplicity of the one-dimensional Winkler foundation models and the accuracy of the approaches based on contact mechanics. For example, in [15] the bump foil was modeled by a system of spring/trusses rigorously reproducing the real structure. However, the structure was considered of infinite axial length. The stiffness matrix was assembled in a manner similar to the finite elements method. The stiffness of the top foil stiffness was initially neglected compared to the stiffness of the bumps. Stick/slip friction forces were considered by using a regularization of Coulomb's law. The model proved to be successful in reproducing the stiffness and the damping of the foil structure. Thereafter, different models were developed and used for the dynamic analysis of foil bearings ([17], [18]).

However, realistic manufacturing errors cannot be analyzed with the approach introduced in [15] because the model considers that all the contacts between the bumps and the top foil or between the bumps and the housing are closed.

The model was improved in [19] and [20] by introducing gaps between the bumps and the top foil, between the bumps and the housing and between the top foil and the rotor. The stiffness of the top foil was also considered as well as the stick-slip effect induced by the Coulomb friction force. This structural model was validated in [19] by comparing the static bump displacements and the resulting stiffness obtained by pushing the rotor into the foil structure. The confrontations with other models were satisfactory and underlined the importance of taking close/loose gaps into account. Further validations of the model for start-up torque, lift-off speed and full steady operating speeds with high static loads were presented in [*20*] and agreed very well with experimental results. Compared to full 3D approaches, the computational effort of this model is orders of magnitude less.

**The analysis of the impact of the manufacturing errors**

The present work is a systematic investigation of the impact of manufacturing errors on the structural stiffness and on the unbalance response. Only the bump height is considered among all the possible manufacturing errors. As in the previous papers, each bump has a different, random height following a normal distribution. Because they belong to the same foil and were obtained by the same manufacturing process, it is natural to consider that the bump heights have the same mean and the same standard deviation. This means that the number of random parameters of the analysis is equal to the number of bumps and is quite high.

The impact of manufacturing errors was already presented in [7], [8] and [19] but only for a very limited number of samples. The goal of the present work is to perform a statistical analysis. The adopted approach is similar to a Monte-Carlo method. This kind of analysis is considered the reference for random phenomena in mechanical problems [21]; it is reliable and its unique problem is the dependence of its accuracy on the number of samples. Other methods based on expansions of the response function could not be used. For example, the polynomial chaos method based on series of orthogonal polynomials with independent Gaussian variables [22] cannot handle a large number random parameters.

The paper presents the most important points of the structural model, of its coupling with the thin air film and the unbalance response of a four degrees of freedom (4dof) rotor supported by a foil bearing and a ball bearing.

A parametric study of the unbalance response of a foil journal bearing with manufacturing errors was performed. The statistical results of each parametric case are estimated from $N$=50…60 samples. This is a small population taking into account that the number of bumps (and therefore of random parameters) is important, generally larger than 20. This limited number of samples cannot yield the exact statistical results and their distribution might not accurately reflect the reality. However, following the central limit theorem, it can yield the mean value and its standard error, $\sigma/\sqrt{N}$, where $\sigma$ is the standard deviation based on $N$ independent results as well as their confidence limits ([23], [24]). More samples, 100, were obtained and analysed for one of the parametric cases to prove the accuracy of the reported results.

## 2. The foil structure model

The unwrapped foil structure is depicted in Figure 3 showing the top and the foils, their degrees of freedom and the close/loose gaps taken into account. Each bump has four degrees of freedom, for example $u_{b1\ldots4}$ and $u_{b5\ldots8}$; $u_{b2,4,6,8}$ are radial displacements while $u_{b1,3,5,7}$ are tangential displacements. The top foil has radial displacements $u_{t1,2}$ etc. corresponding to the top of each bump. Its stiffness matrix, $\boldsymbol{K_t}$, is estimated by using Bresse's equations for a curved beam.

The corrugated bum foil is modeled by using a system of springs depicted in Figure 4. Each bump is described by three springs of stiffness $k_1$ and $k_2$ and other springs of stiffness $k_3$ and $k_4$ connect the bumps. The stiffness $k_{1\ldots4}$ are deduced from Castaigliano's relation. The bumps are then assembled into a global stiffness matrix $\boldsymbol{K_b}$ in a manner similar to the finite element method. The bump and the top foil stiffness matrices were presented in [19] and [20] and are now omitted for brevity.

The gaps that are taken into account are:

- the gap between the rotor and the top foil: $g_{r,i} = C_r + x_r cos\theta_i + y_r sin\theta_i + u_{t,i} \geq 0$ ( 1)
- the gap between the top foil and the bump foil: $g_{t,i} = g_{0_{t,i}} - u_{t,i} + u_{b,1+2(i-1)} \geq 0$ ( 2)
- the gap between the bump foil and the sleeve: $g_{b,i} = g_{0_{b,i}} - u_{b,2+2(i-1)} \geq 0$ ( 3)

If non-zero, the initial gaps, $g_{0_{t,i}}$ and $g_{0_{b,i}}$ can describe manufacturing errors of the foil structure. Following the non-interference condition, all gaps must positive (open/loose) or null (closed). This is mathematically described by the Signorini-Moreau condition [25].

$$g_i \geq 0 \wedge F_{n,i} \leq 0 \wedge g_i F_{n,i} = 0 \tag{4}$$

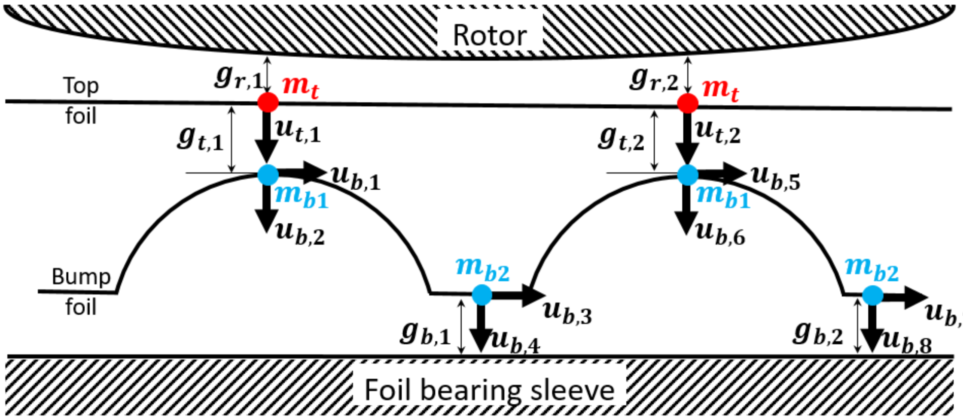

*Figure 3 : Gaps and degrees of freedom of the structural model*

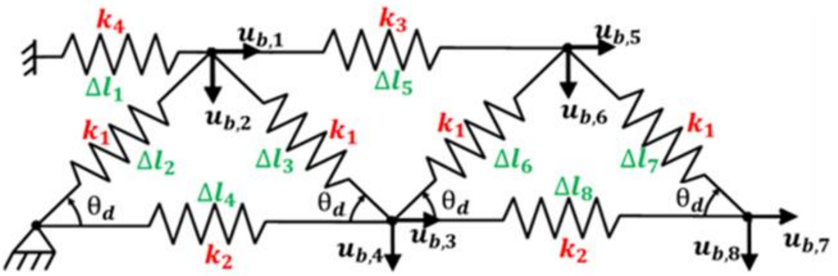

*Figure 4 : Discretization of the bump foil with 4DOF per bump.*

The potential energy of the structure with gaps must consider these constraints. The normal contact forces are calculated by using the augmented Lagrange multipliers method for the bump/top foil contacts and for the bump/sleeve contacts and the penalty method for the rotor/top foil contacts. The potential energy of the foil structure is then:

$$\begin{aligned}\Pi_{ALM} = &\frac{1}{2}\boldsymbol{u_b}^T\boldsymbol{K_b}\boldsymbol{u_b} + \frac{1}{2}\boldsymbol{u_t}^T\boldsymbol{K_t}\boldsymbol{u_t} + \sum_{i=1}^{N_{cntct}}\left(\bar{\lambda}_i g_i + \frac{1}{2}\varepsilon_{ALM} g_i^2\right) + \frac{1}{2}\sum_{i=1}^{N_{Rotor}} \varepsilon_r g_{r,i}^2 \\ &+ \frac{1}{2}\sum_{i=1}^{N_{stick}} \varepsilon_f \left(u_{b,i} - u_{b,i}^{(0)}\right)^2 - \sum_{i=1}^{N_{slip}} \underbrace{f\bar{\lambda}_i sign\left(\dot{u}_{b,i}\right)}_{F_{f,i}} \left(u_{b,i} - u_{b,i}^{(0)}\right)\end{aligned} \tag{5}$$

where $N_{cntct}$ is the number of contact between foils and between the corrugated foil and the bearing sleeve. $N_{Rotor}$is the number of contacts between the top foil and the rotor. $N_{stick}$ and $N_{slip}$ are successively numbers of contacts in stick state and slip state. $\bar{\lambda}_i = F_{n,i} \leq 0$ is the normal contact force. $\varepsilon_{ALM}$ is the augmented Lagrange multiplier. $\varepsilon_r$ and $\varepsilon_f$ are the penality coefficients for successively the contact between the rotor/top foil and top foil/bumped foil or bumped foil/bearing sleeve.

Friction forces at closed bump/top foil and bump/sleeve contacts are also added to the potential energy. They are calculated with the penalty method for stick contacts and with the Coulomb law for slip contacts. The Lagrange multipliers in eq.

( 5) correspond to normal contact forces, $\bar{\lambda}_i = F_{n,i} \leq 0$.

The equations obtained by minimizing the potential energy (4) yield:

$$\begin{bmatrix} \boldsymbol{K_b} + \boldsymbol{L_{bb}} & \boldsymbol{L_{bt}} \\ \boldsymbol{L_{bt}^T} & \boldsymbol{K_t} + \boldsymbol{L_{tt}} \end{bmatrix} \begin{Bmatrix} \boldsymbol{u_b} \\ \boldsymbol{u_t} \end{Bmatrix} = \begin{Bmatrix} \boldsymbol{F_b} \\ \boldsymbol{F_t} \end{Bmatrix} \tag{6}$$

In this equation, $\boldsymbol{L_{bb}}$, $\boldsymbol{L_{bt}}$, $\boldsymbol{L_{tt}}$ are the coupling matrices and $\boldsymbol{F_b}$ and $\boldsymbol{F_t}$ are vectors containing the Lagrange multipliers and the penalties. This equation is non-linear because the vector $\boldsymbol{F_b}$ contains terms of the kind $\bar{\lambda}_i sign(\dot{u}_{b,i})$.

## Impact of the bump height manufacturing errors on the foil structure stiffness and energy loss

The geometrical and material characteristics of the foil bearing depicted in Figure 1 are given in Table 1.

*Table 1: Geometric and mechanical characteristics of the foil*

| | |
|---|---|
| Foil bearing axial length, L | 38.1 mm |
| Number of bumps | 26 |
| Rotor radius, *R* | 19.05 mm |
| Radial clearance, $C_r$ | 31.8 µm |
| Nominal bump height, $h_b$ | 0.508 mm |
| Foil thickness (of the bumped foil $e_b$, and of the top foil $e_t$) | 0.102 mm |
| Young modulus, *E* | 214 GPa |
| Poisson's ratio, *ν* | 0.29 |
| Bump length, $2l_0$ | 3.556 mm |
| Used thin layer fluid | Perfect gas |

The foil structure stiffness and its energy loss are estimated by incrementally pushing the journal into the compliant bearing.

Figure 5 depicts the force versus the positive X displacement (i.e. opposite to the welding point) for the foil structure free of manufacturing errors and for two cases with bump height manufacturing errors, HBE1 and HBE2. The results were obtained for a friction coefficient of 0.3 and the maximum

displacement is 2.5 time the radial clearance. The bump height errors of the cases presented in Figure 5 have a standard deviation of 5% of the nominal bump height.
The loading curve yields a stiffness of the foil structure while the area comprised between the two curves characterizes the energy loss. The stiffness of the bump foil is non-linear; in the following, its value at the maximum considered displacement (i.e. 80 µm) will be used for comparisons.

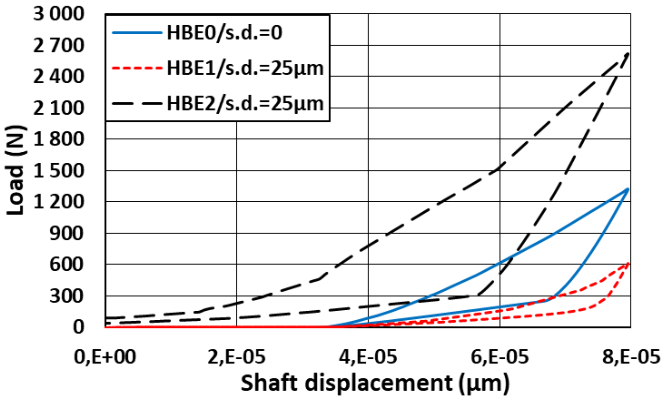

*Figure 5: Load versus rotor static displacement*

Figure 6 depicts the mean value of the structural stiffness obtained based on 50 samples and for different friction coefficients (0, 0.1, 0.2 and 0.3). Standard deviations of the bump heights comprised between 1% and 10% of the nominal (design) height were explored. The mean value of the stiffness increases with the friction coefficient and decreases very weakly with the magnitude of the bump height-manufacturing errors. However, its standard deviation increases with both the friction coefficient and the magnitude of the manufacturing errors.

Figure 7 depicts the mean energy loss. Both the mean value and the standard deviation of the energy loss increase with the friction coefficient and the magnitude of the bump height-manufacturing errors.

The ratios between the standard deviation and the mean value of the foil stiffness and of the energy loss versus the bump height-manufacturing errors are depicted in Figure 8. They increase linearly with the magnitude of the manufacturing errors and the linear approximation do not depend on the friction coefficient. The greater increase in energy loss shows that it is more sensitive to manufacturing errors.

This is true for all load directions. For example, the results obtained for +X and +Y rotor displacements and a friction coefficient of 0.3 are depicted in Figure 9. The linear variation of the ratio between the standard deviation and the mean value is obtained also for the +Y direction.

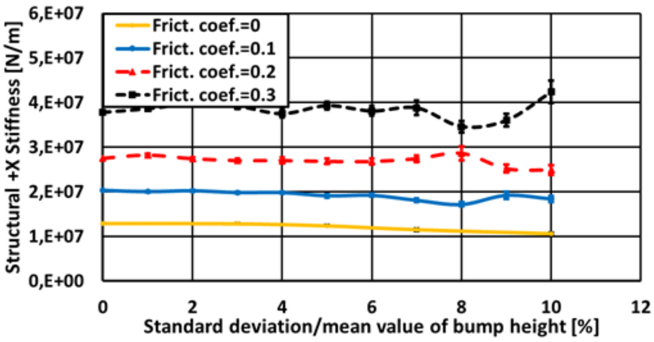

*Figure 6: Variation of the structural stiffness with the standard deviation of bump heights*

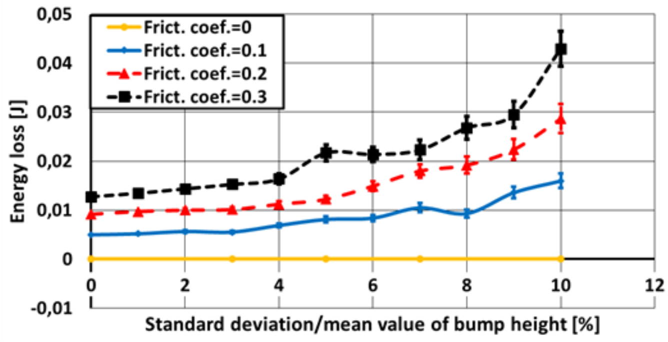

*Figure 7: Variation of the loading/unloading dissipated energy with the standard deviation of bump heights*

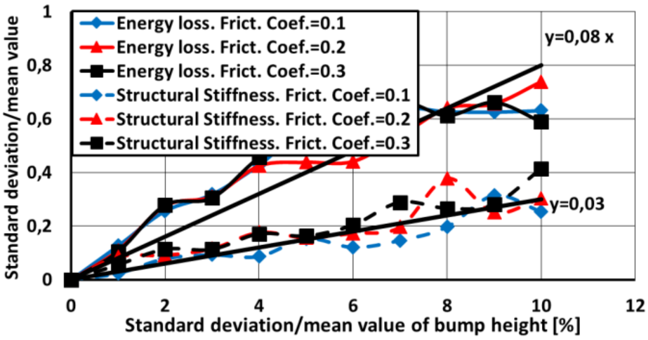

*Figure 8: Variation of the standard deviation/mean value with the standard deviation of bump heights*

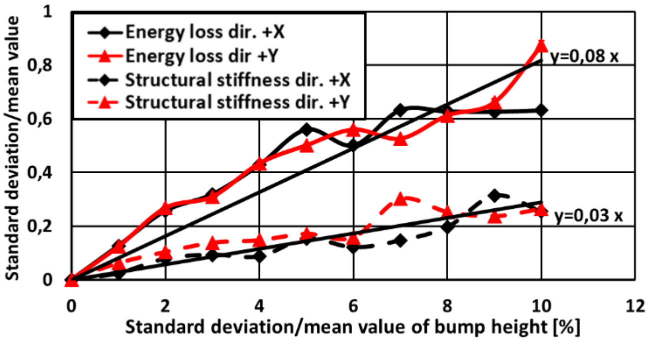

*Figure 9: Variation of the standard deviation/mean value with the standard deviation of bump heights in +X and +Y directions (frict. coeff.=0.3)*

## 3. The aerodynamic foil bearing model

The second part of the aerodynamic foil bearing model is the coupling of the structural model with the thin gas film flow between the shaft and the top foil. The compressible thin film flow is described by Reynolds equation for an ideal gas operating under isothermal conditions [26].

$$\frac{\partial}{\partial x}\left(\frac{\tilde{P}h^3}{12\mu}\frac{\partial P}{\partial x}\right)+\frac{\partial}{\partial z}\left(\frac{\tilde{P}h^3}{12\mu}\frac{\partial P}{\partial z}\right)=\frac{R\Omega}{2}\frac{\partial\left(\tilde{P}h\right)}{\partial x}+\frac{\partial\left(\tilde{P}h\right)}{\partial t} \quad (7)$$

where $\tilde{P}$ are “upwinded” pressures. The ambient pressure is imposed along the axial welding (Figure 1) and at the two ends of the bearing. The equation is discretized following the finite volume method on a rectangular grid corresponding to the unwrapped bearing. The discretized system of equations is non-linear due to $\tilde{P}$ and is solved by using the Newton-Raphson method. Equation (7) is not sufficient for modelling the pressures between the top and the rotor. If the local film thickness is smaller than three times the equivalent standard deviation of the roughness heights, then contacts between roughness asperities may occur. The mixed lubrication regime is then considered by calculating a local contact pressure $P_{cntct}$ following a statistical contact model (a.e. Grenwood and Williamson, [27]).

For coupling the structural model with Reynolds equation the variation of the bump and top foils stiffness in the axial direction is discarded. The two-dimensional pressures calculated from Reynolds equation and from the contact model are axially averaged:

$$P_{ax} = \frac{1}{L}\int_0^L (P + P_{cntct})dz \tag{8}$$

The corresponding radial force that loads the top foil is:

$$dF = \left(P_{ax} - P_{ext}\right)Rd\theta L \tag{9}$$

While the forces acting on the rotor are:

$$F_x = \int_0^{2\pi} dFcos\theta, F_y = \int_0^{2\pi} dFsin\theta \tag{10}$$

The assumption that an axially averaged pressure loads the top foil is coherent with the structural model but it supposes that the thin film thickness is constant in the axial direction. This is not exactly true in aerodynamic foil bearings where the pressure varies axially from the mid plane to the bearing ends for satisfying the boundary condition, $\mathrm{P} = \mathrm{P}_{\mathrm{ext}}$ @ $\mathrm{z} = \pm \mathrm{L}/2$. The real film thickness has a similar variation, decreasing from a maximum value at the mid plane to a minimum value at the bearing ends. Experimental results showed a systematic wear of the foils at the bearing ends. Considering the axial direction in the structural model of the foils would lead to approaches of the kind presented in [7] and [8] while the goal of the present model is to computationally more efficient. The modelling assumption of an axially constant thin film thickness is therefore the condition for a simple structural model and the thin film thickness will then be the gap given by eq. (1).

The second point in coupling the structural model with the thin film pressure field is to distinguish the discretization points of the top foil among the discretization cells of Reynolds equations. The situation is depicted in Figure 10.

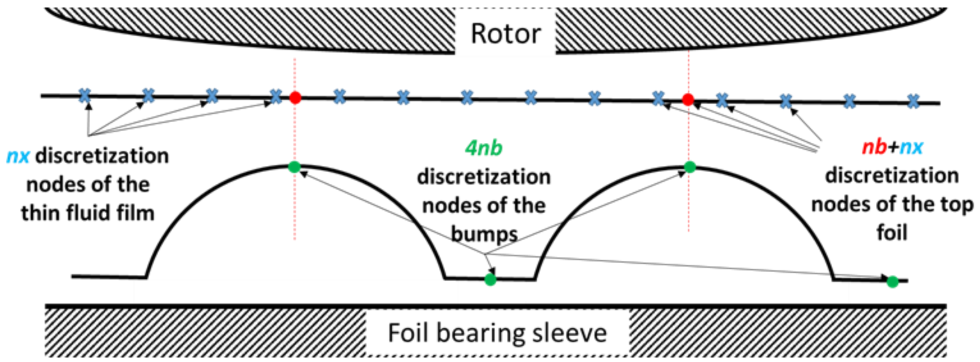

Figure 10: Circumferential discretization of the top and bump foils

The discretization points of the top foil correspond to the top of the bumps. The number of circumferential discretization points of Reynolds equation is at least the double of the number of bumps, *nb*. In the present structural model, the stiffness matrix of the bump foil has *4nb* lines and columns. The stiffness matrix of the top foil is obtained by considering the *nb* bumps and the *nx* discretization lines of Reynolds equation organised in increasing circumferential direction. However, the contact algorithm requires a clear distinction between the *nb* nodes where contacts may occur and the rest. Therefore, the stiffness matrix and the degrees of freedom of the top foil are re-organized as its follows.

$$[\boldsymbol{K}_t] = \begin{bmatrix} \boldsymbol{K}_{t11} & \boldsymbol{K}_{t12} \\ \boldsymbol{K}_{t12}^T & \boldsymbol{K}_{t22} \end{bmatrix}, \{\boldsymbol{u}_t\} = \begin{Bmatrix} \boldsymbol{u}_{t1} \\ \boldsymbol{u}_{t2} \end{Bmatrix} \tag{11}$$

Where $\boldsymbol{u}_{t1}$ are the *nb* degrees of freedom of the top foil associated to the bumps (where gaps are defined and contacts may occur) and $\boldsymbol{u}_{t2}$ are the *nx* degrees of freedom associated with the discretization lines of the Reynolds equation. The complete non-linear system of equation replacing eq. (6) is now:

$$\begin{bmatrix} \boldsymbol{K}_b + \boldsymbol{L}_{bb} & \boldsymbol{L}_{bt} & \boldsymbol{0} \\ \boldsymbol{L}_{tb}^T & \boldsymbol{K}_{t11} + \boldsymbol{L}_{tt} & [\boldsymbol{K}_{t12}]_{nb,nx} \\ \boldsymbol{0} & \boldsymbol{K}_{t12}^T & \boldsymbol{K}_{t22} \end{bmatrix} \begin{Bmatrix} \boldsymbol{u}_b \\ \boldsymbol{u}_{t1} \\ \boldsymbol{u}_{t2} \end{Bmatrix} = \begin{Bmatrix} \boldsymbol{F}_b \\ \boldsymbol{F}_{t1} + \boldsymbol{F}_{p1} \\ \boldsymbol{F}_{p2} \end{Bmatrix} \tag{12}$$

The system is decomposed into two sub-problems:

$$\underbrace{\left(\boldsymbol{K}_{bt1} - \boldsymbol{L}_{t12}\boldsymbol{K}_{t22}^{-1}\boldsymbol{L}_{t21}\right)}_{\boldsymbol{K}_{bt}} \boldsymbol{u}_{bt1} = \underbrace{\boldsymbol{F}_{bt1} - \boldsymbol{L}_{t12}\boldsymbol{K}_{t22}^{-1}\boldsymbol{F}_{p2}}_{\boldsymbol{F}_{bt}} \tag{13}$$

$$\boldsymbol{K}_{bt1} = \begin{bmatrix} \boldsymbol{K}_b + \boldsymbol{L}_{bb} & \boldsymbol{L}_{bt} \\ \boldsymbol{L}_{tb} & \boldsymbol{K}_{t11} + \boldsymbol{L}_{tt} \end{bmatrix}, \boldsymbol{u}_{bt1} = \begin{Bmatrix} \boldsymbol{u}_b \\ \boldsymbol{u}_{t1} \end{Bmatrix}, \boldsymbol{F}_{bt1} = \begin{Bmatrix} \boldsymbol{F}_b \\ \boldsymbol{F}_{t1} + \boldsymbol{F}_{p1} \end{Bmatrix} \tag{14}$$

$$\boldsymbol{u}_{t2} = \boldsymbol{K}_{t22}^{-1}\left(\boldsymbol{F}_{p2} - \boldsymbol{L}_{t21}\boldsymbol{u}_{bt1}\right) \tag{15}$$

where eq. (13) and (15) represent systems of non-linear and linear systems of equations, respectively. The system is solved following a special algorithm that detects closed/loose gaps and stick/slip contacts. The algorithm first detects if the gaps are closed or loose depending on the initial values of the displacements. The augmented Lagrange multipliers $\bar{\lambda}$ have zero initial values. If gaps are closed, then they are supposed to be in stick state and a first estimation of the friction forces is calculated using the penalty method.

$$F_f^{trial} = \varepsilon_f \left( u_b - u_b^{(0)} \right) \tag{16}$$

Where $u_b^{(0)}$ is the displacement at the previous loading step. The non-linear system of equations (13) is solved using a Newton-Raphson algorithm. This is the innermost loop of the algorithm. The solution yields the new values of the displacements, $\boldsymbol{u_b}$, $\boldsymbol{u_{t1}}$ and $\boldsymbol{u_{t2}}$.

The algorithm then checks if the contacts are in stick or slip state.

$$\begin{cases} if\ \left|F_f^{trial}\right| < f\left|\bar{\lambda}\right|\ then\ F_f^{(k)} = F_f^{trial}, stick\ state \\ otherwise\ F_f^{(k)} = f\bar{\lambda} sign\left(\dot{u}_{tg}^{(k)}\right), slip\ state \end{cases} \tag{17}$$

and the solution of the non-linear system of equations (13) is repeated until the convergence of the friction forces. This is the second loop of the algorithm. The values of the augmented Lagrange multipliers are kept constant during the calculation of the friction forces. Once the friction forces are converged, the augmented Lagrange multipliers are updated:

$$\bar{\lambda}_i^{(n+1)} = \bar{\lambda}_i^{(n)} + \varepsilon_{ALM} g_i^{(n+1)} \tag{18}$$

and the whole algorithm is repeated until convergence. This is the third loop of the algorithm. After the convergence of the augmented Lagrange multipliers the close/loose state of the contacts is checked. The whole calculation is repeated if the initial assumption of close/loose state is not verified.

The algorithm consists of four embedded loops and proceeds in an iterative manner. The key point ensuring the robustness of the contact algorithm is keeping the augmented Lagrange multipliers (i.e. the normal contact forces) constant while calculating the friction forces.

Once the algorithm is converged the film thickness is calculated in all points following eq. (1), i.e. $h_i = g_{r,i}$. It should be underlined that defining the film thickness as a gap and treating it subsequently avoids any artificial (i.e. numerical) interpenetration between the top foil and the rotor.

## Dynamic analysis. Impact of manufacturing errors on the unbalance response of a 4DOF rotor

The classic method for the unbalance response of rotors supported by journal bearings is expressing the hydrodynamic forces via dynamics coefficients [26]. These coefficients are obtained by using the small perturbation assumption. It is then supposed that the dynamic amplitudes are small compared to the radial clearance. This assumption is most often not valid for aerodynamic foil bearings because, as shown in Figure 5, the stiffness of their structure is non-linear and because the friction induced damping depends on the magnitude of the dynamic amplitudes. The best practice is then a full non-linear analysis based on the time integration of the equations of motion of the rotor-bearing system.

The coupling between the unsteady Reynolds equation (7) and the dynamic of the top foil must be explained a priori. The implicit integration of the discretized unsteady Reynolds equation raises no problem if the film thickness given by (1) is known. The dynamic behavior of the top foil can be described by an equation of motion of the kind:

$$\boldsymbol{M}\ddot{\boldsymbol{u}}_{\boldsymbol{bt1}} + \boldsymbol{C}\dot{\boldsymbol{u}}_{\boldsymbol{bt1}} + \boldsymbol{K}\boldsymbol{u}_{\boldsymbol{bt1}} = \boldsymbol{F} \tag{19}$$

The stiffness matrix $\boldsymbol{K}$ and the vector of external forces applied on the structure $\boldsymbol{F}$ were defined by eq. (12):

$$\boldsymbol{K} = \boldsymbol{K}_{\boldsymbol{bt1}} - \boldsymbol{L}_{\boldsymbol{t12}}\boldsymbol{K}_{\boldsymbol{t22}}^{-1}\boldsymbol{L}_{\boldsymbol{t21}} \tag{20}$$

$$\boldsymbol{F} = \boldsymbol{F}_{\boldsymbol{bt1}} - \boldsymbol{L}_{\boldsymbol{t12}}\boldsymbol{K}_{\boldsymbol{t22}}^{-1}\boldsymbol{F}_{\boldsymbol{p2}} \tag{21}$$

The mass matrix of the compliant structure is build with the mass matrices of the bump and top foils:

$$\boldsymbol{M} = \begin{bmatrix} \boldsymbol{M}_{\boldsymbol{b}} & 0 \\ 0 & \boldsymbol{M}_{\boldsymbol{t}} \end{bmatrix} \tag{22}$$

A simplified estimation of these matrices using a model based on lumped masses is possible as suggested in Figure 3. For example:

$$\boldsymbol{M}_{\boldsymbol{t}} = DIAG\{m_t \quad \cdots \quad m_t\} \tag{23}$$

$$\boldsymbol{M}_{\boldsymbol{b}} = DIAG\{m_{b1} \quad m_{b1} \quad m_{b2} \quad m_{b2} \quad \cdots \quad m_{b1} \quad m_{b1} \quad m_{b2} \quad m_{b2}\} \tag{24}$$

Mass matrices can then be instantly inverted. The damping matrix in (19) could be estimated following a Rayleigh type structural damping but its contribution would be limited.

Models based on non-linear elasticity commercial codes showed that using eq. (19) for the dynamic response of the structure requires very small time steps. The requirement holds for explicit as well as for implicit time integration algorithms because all the time scales of the discretized structure must be resolved when using eq. (19). This is the main reason for the long calculation time reported in [7] and [8]. Therefore, a more simple approach was adopted: the mass and the damping matrices were discarded in eq. (19) and therefore the eigenmodes of the structure were not modeled. This allowed the use of much larger time steps.

For example, the equations of motion of a two degrees of freedom (2dof) rotor-bearing system are:

$$M_R \begin{Bmatrix} \ddot{x} \\ \ddot{y} \end{Bmatrix} = \begin{Bmatrix} F_x \\ F_y \end{Bmatrix}_{(x,y,\dot{x},\dot{y})} + M_R e_B \Omega^2 \begin{Bmatrix} cos(\Omega t) \\ sin(\Omega t) \end{Bmatrix} + \begin{Bmatrix} W_x \\ W_y \end{Bmatrix} \tag{25}$$

with the initial conditions, $x = y = \dot{x} = \dot{y} = 0 \ @ \ t = 0$. This system of equations can be time integrated by using either implicit or explicit methods. Foil bearing forces must be calculated at least once at each time step. This means that Reynolds equation (7) and the model of the foil structure (12) are time integrated in a coupled manner. Implicit methods are often preferred because they do not suffer from time step stability limitations. The time step is controlled only by the desired accuracy of the result. In the meantime, the bearing forces are non-linear because they depend on the state variables, $x, y, \dot{x}, \dot{y}$. This means that a non-linear algorithm must be applied at each time step. Repeated calculations of the bearing forces proved to be very time consuming and therefore the use of an implicit algorithm was abandoned.

The explicit algorithm requires only a single estimation of the bearing forces per time step. However, the numerical accuracy of an explicit time integration algorithm is more difficult to control than an implicit algorithm. For a rigorous control, the calculations should be repeated at each step with different values of the time increment and the results compared. This would lead to very lengthy calculations with repeated estimations of foil bearing forces at each time step. Therefore, the accuracy of the time integration was only a posteriori verified.

Figure 11 depicts a non-linear stability analysis performed using eq. (25). The foil bearing had the characteristics given in Table 1 and $M_R$=1 kg, $W_x$=30 N, $W_y$=0, Ω=30 krpm, $e_B$=0. The results were obtained for three different time steps $\Delta t$=$T/512$, $T/1024$ and $T/2048$where $T = 2\pi/\Omega$. The results obtained with $\Delta t$=$T/1024$ and $T/2048$ are very close at all-time steps. The results obtained with $\Delta t$=$T/512$ show differences in the first time steps when the accelerations are large but tend to the same values of the displacements when time progresses. The results obtained with $\Delta t$=$T/1024$ were therefore considered accurate.

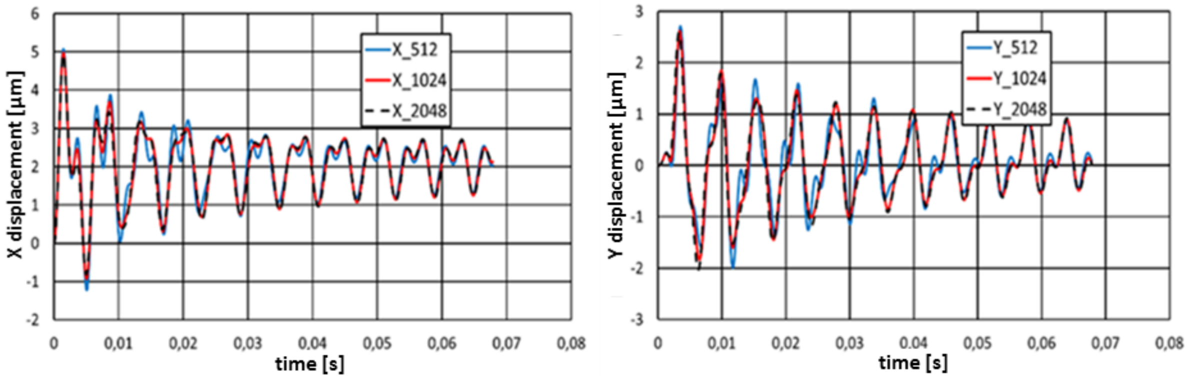

*Figure 11 : Dynamic displacements of the 2d.o.f. rotor calculated with different time steps*

## Impact of manufacturing errors on the unbalance response of a a 4DOF rotor

The two degrees of freedom model based on the Jeffcott rotor is somewhat artificial for investigating the impact of manufacturing errors because the two foil bearings are rigorously identic. A more realistic model of a rigid rotor supported at its ends by a ball bearing and by a foil bearing was therefore considered [28]. The system had four degrees of freedom.

$$\begin{cases} M_R\ddot{x}_G = F_x^1 + F_x^2 + W_X + M_R e_B \Omega^2 cos(\Omega\mathrm{t}) \\ M_R\ddot{y}_G = F_y^1 + F_y^2 + W_Y + M_R e_B \Omega^2 sin(\Omega\mathrm{t}) \\ I_d\ddot{\theta}_r + I_p\Omega\dot{\psi} = \delta_1 F_y^1 + \delta_2 F_y^2 + M_R e_B \Omega^2 \delta_b sin(\Omega\mathrm{t}) \\ I_d\ddot{\psi} - I_p\Omega\dot{\theta}_r = -\delta_1 F_x^1 - \delta_2 F_x^2 - M_R e_B \Omega^2 \delta_b cos(\Omega\mathrm{t}) \end{cases} \tag{26}$$

The displacements at the bearings centers are:

$$x_k \approx x_G + \delta_k\psi, y_k \approx y_G - \delta_k\theta_r, k = \{1,2\} \tag{27}$$

Similar relations hold for velocities at the bearings centers.

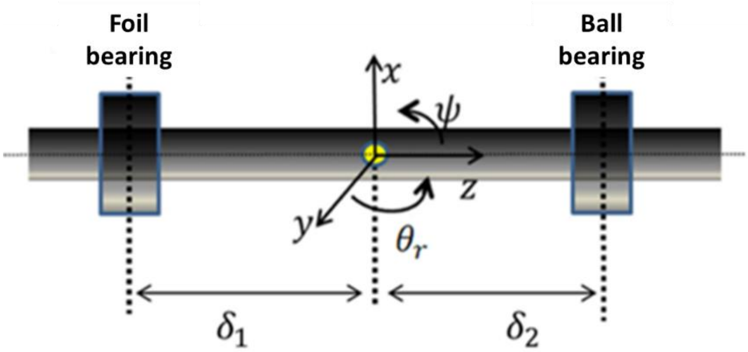

*Figure 12 : Notations and coordinate system for a rigid rotor*

The e.o.m. are expressed as a system of first order differential equations.

$$\begin{Bmatrix} \dot{\boldsymbol{q}} \\ \ddot{\boldsymbol{q}} \end{Bmatrix} = \begin{bmatrix} \mathbf{0} & \boldsymbol{I}^{4\times 4} \\ \mathbf{0} & -\boldsymbol{M}^{-1}\boldsymbol{G} \end{bmatrix} \begin{Bmatrix} \boldsymbol{q} \\ \dot{\boldsymbol{q}} \end{Bmatrix} + \begin{Bmatrix} \{0\}_4 \\ F_x^1 + F_x^2 + W_X + M_R e_B \Omega^2 cos(\Omega\mathrm{t}) \\ F_{y1} + F_{y2} + W_Y + M_R e_B \Omega^2 sin(\Omega\mathrm{t}) \\ \delta_1 F_y^1 + \delta_2 F_y^2 + M_R e_B \Omega^2 \delta_b sin(\Omega\mathrm{t}) \\ -\delta_1 F_x^1 - \delta_2 F_x^2 - M_R e_B \Omega^2 \delta_b cos(\Omega\mathrm{t}) \end{Bmatrix} \tag{28}$$

$$\boldsymbol{q} = \begin{Bmatrix} x_G \\ y_G \\ \theta_r \\ \psi \end{Bmatrix}, \boldsymbol{M} = \begin{bmatrix} M_R & 0 & 0 & 0 \\ 0 & M_R & 0 & 0 \\ 0 & 0 & I_d & 0 \\ 0 & 0 & 0 & I_d \end{bmatrix}, \boldsymbol{G} = \begin{bmatrix} 0 & 0 & 0 & 0 \\ 0 & 0 & 0 & 0 \\ 0 & 0 & 0 & I_p\Omega \\ 0 & 0 & -I_p\Omega & 0 \end{bmatrix} \tag{29}$$

that are integrated following an explicit Euler method with initial conditions, $\boldsymbol{q} = \dot{\boldsymbol{q}} = 0 \ @ \ t = 0$.

The inertia characteristics of the rotor are $M_R$ =2 kg, $I_p$=0.0175 kgm$^2$, $I_d$=0.0032 kgm$^2$. The foil bearing and the ball bearing are equally spaced from the center of mas, $\delta_1$=-$\delta_2$=0.1 m. Different unbalances were considered at the rotor center of mass. The ball bearing has a stiffness $K_{bb}$=2.5·10$^8$ N/m and a structural damping $\eta_{bb}$=0.5%, both constant with the rotation speed. Calculations were performed for distinct rotation speeds comprised between 5 krpm and 55 krpm. Each calculation was performed for a time interval corresponding to 200 periods of the rotation speeds. Generally, the orbits became stabilized after 100 periods. In all cases, the stabilized orbits showed only synchronous responses.

The results obtained for two sets of random bump heights (HB1, HB2 of Figure 5) and for two magnitudes of the manufacturing errors (standard deviations of 1% and 2% of the design bump height, i.e. 5 µm and 10 µm) are depicted in Figure 13. The results are compared with the case without manufacturing errors, HB0.

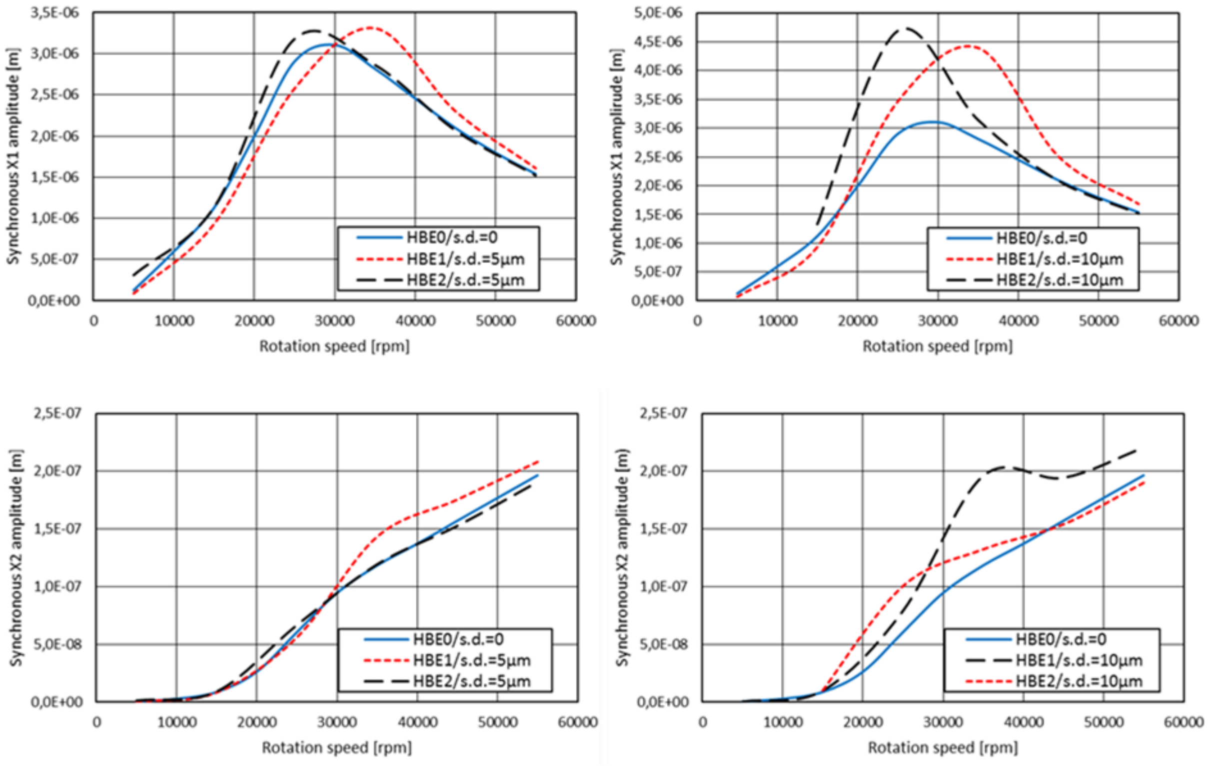

*Figure 13 : Synchronous amplitudes following X direction of the unbalance response of the 4dof rotor-bearing system.*

The top left Figure 13 shows the X amplitudes in the foil bearing. The critical speed of the conical forward mode is visible just before 30 krpm for the HB0 case. Adding 5% bump height manufacturing errors modifies the critical speed either increasing or decreasing it. This observation is reinforced by the top right Figure 13 showing the amplitudes in the foil bearing for the cases with errors of 10 µm standard deviation. Compared to the cases with 5 µm bump height errors, the critical speeds are not modified but the synchronous amplitudes at critical speed increased considerably. These results show that the damping of the foil bearing varies non-linearly with the bump height manufacturing errors.

The amplitudes in the ball bearing are depicted in the lower left and right part of Figure 13. The values of the synchronous amplitudes are much smaller than in the foil bearing and increase continuously with the rotation speed.

Figure 14 depicts the synchronous X amplitudes in the foil bearing obtained with two other unbalance values, 0.1 gmm and 0.5 gmm and the same manufacturing errors profiles. These results confirm that the amplitude at critical speed is more sensitive to the magnitude of the bump height manufacturing errors than the critical speed.

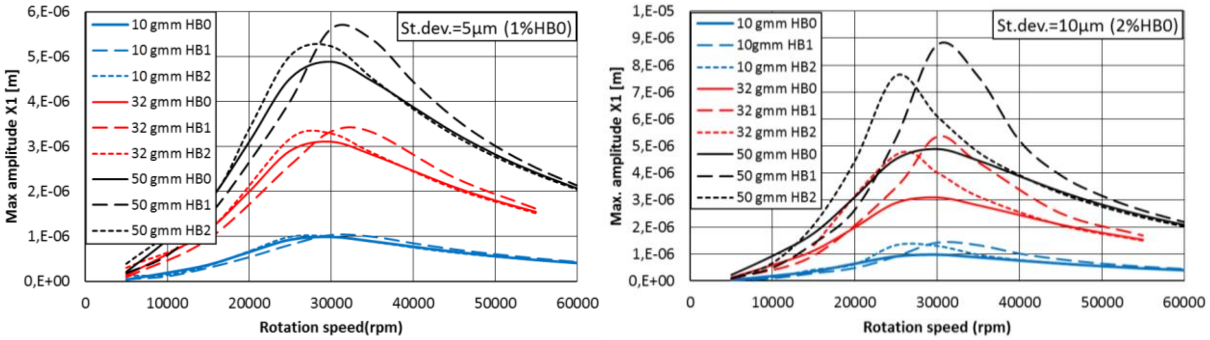

*Figure 14: Synchronous X amplitudes of the foil bearing from the unbalance response of the 4dof rotor-bearing system*

Figure 15 and Figure 16 depict the mean values and the dimensionless standard deviations obtained from $N$=50…60 independent manufacturing errors profiles. Three values of the unbalance (0.1 gmm, 0.32 gmm and 0.5 gmm) were used and each manufacturing error profile was attributed two standard deviation (5 µm and 10 µm, i.e. 1% and 2% of the design value). The markers depicted in Figure 15 and Figure 16 correspond to the lower and upper limit of the interval of confidence of 95% ([23], [24]). For the mean values of the critical speed and of the maximum amplitudes the interval of confidence was calculated from the standard error of the mean, $\sigma/\sqrt{N}$, and Student's t distribution, for example:

$$\bar{\Omega}_{cr} \in \left[\bar{\Omega}_{cr} \pm \frac{\sigma_{\Omega\mathrm{cr}}}{\sqrt{N}} t_{N-1}(2.5\%)\right] \tag{30}$$

For the values of the standard deviation, the limits of the interval of confidence of 95% were obtained from the chi-squared distribution:

$$\sigma^2 \in \left[\frac{(N-1)\sigma^2}{\chi^2_{2.5\%}}, \frac{(N-1)\sigma^2}{\chi^2_{97.5\%}}\right] \tag{31}$$

Figure 15 shows that the magnitudes of the unbalance and of the manufacturing errors have a negligible influence on the mean value of the critical speed. However, the standard deviation of the critical speed is sensitive to the magnitude of the manufacturing errors, its values being up to 10% of the mean critical speed.

Figure 16 depicts the statistical results for the synchronous amplitude at critical speed. The results show that the mean value of the amplitude increases with the magnitude of the manufacturing errors. Its standard deviation divided by the mean value is also magnified by the manufacturing errors.

The synchronous amplitudes are more sensitive to manufacturing errors than the critical speeds; their standard deviations divided by the mean values are comprised between 10% and 23% compared to 8% to 10% for the critical speeds. The 95% intervals of confidence are also larger.

In all cases, the standard deviations obtained for $N$=50…60 samples can be quite high. The histograms for the 32 gmm unbalance and 1% magnitude of the manufacturing errors are depicted in Figure 17 and show that the limited number of samples have not an exact normal distribution.

For this case, the calculations were continued for a larger number of samples, 100, in order to verify the accuracy the results reported in Figure 15 and Figure 16 and based on 50 to 60 samples. Figure 17 compares the histograms obtained with 60 and 100 samples. Changing the histograms to a normal distribution when increasing the number of samples from 60 to 100 is marginal.

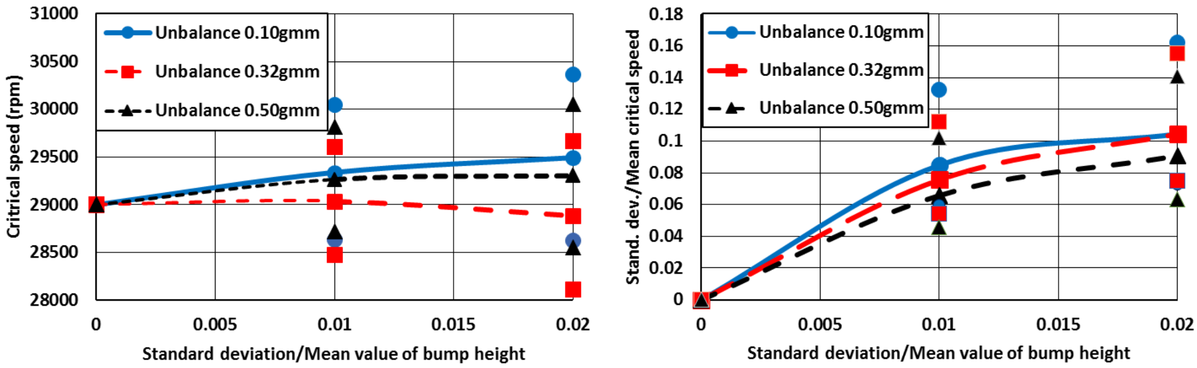

*Figure 15: Mean value and dimensionless standard deviation of the (first) critical speed of the 4d.o.f. rotor*

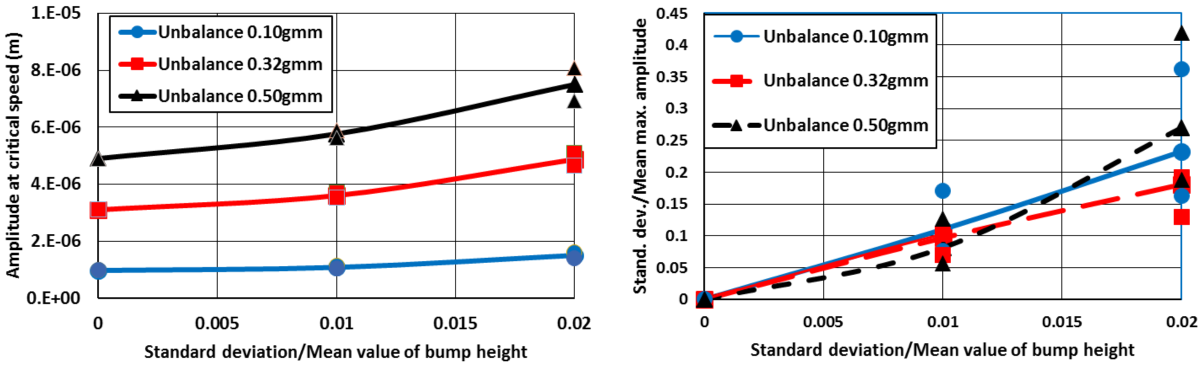

*Figure 16: Mean value and dimensionless standard deviation of the synchronous X amplitudes of the foil bearing at the (first) critical speed*

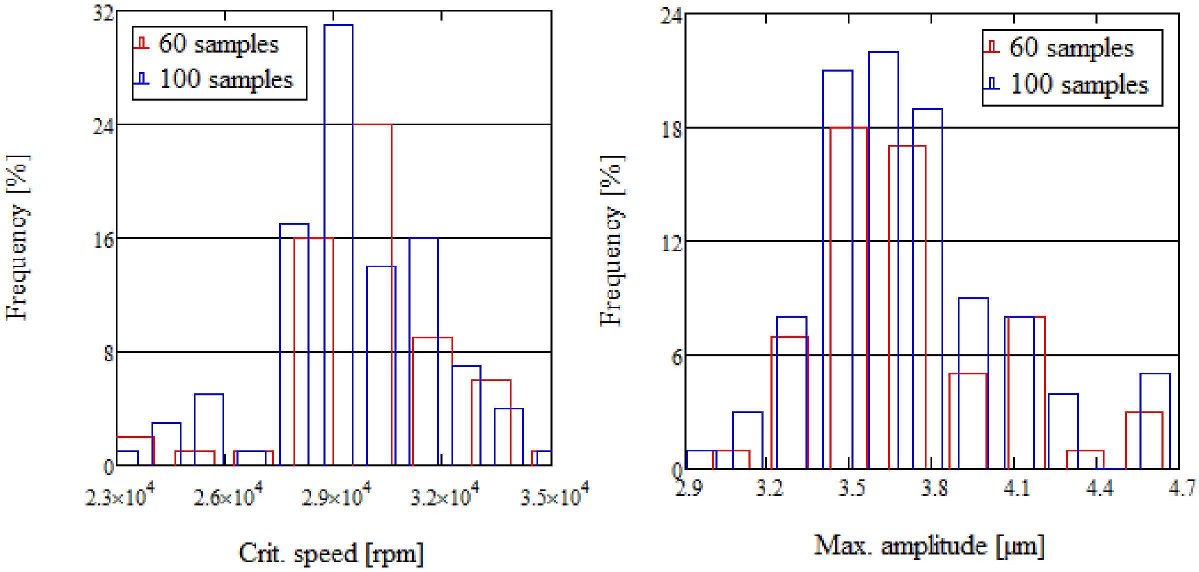

*Figure 17: Histograms of the critical speed and of X maximum amplitudes (0,32 gmm unbalance and 1% magnitude of the manufacturing errors)*

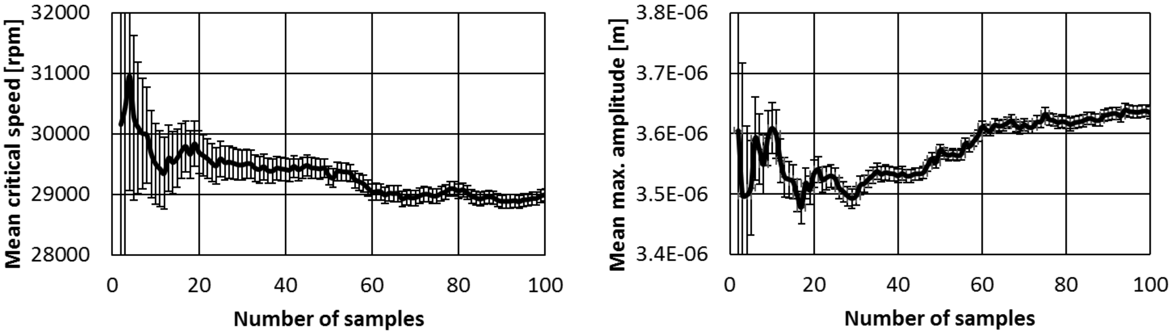

*Figure 18: Mean critical speed and X maximum amplitude vs. the number of samples (0,32 gmm unbalance and 1% magnitude of the manufacturing errors)*

A better insight is given by Figure 18 depicting the variations of the mean critical speed and of the maximum amplitude with the number of samples as well as the interval of confidence of 95%. The increase of the number of samples from 60 to 100 brought minor modifications of the mean values. The major variations with the largest uncertainties occur for the first 40 to 60 samples.

## 4. Conclusions

The paper presents a systematic investigation of bump height manufacturing error on the structural characteristics and on the unbalance response of an aerodynamic foil bearings. The unbalance response is described by the critical speed and the amplitude of the first mode of a 4 d.o.f. rotor supported by a ball bearing and an aerodynamic foil journal bearing. The results were obtained by non-linear unbalance response calculations. They show that the bump height manufacturing errors have a small impact on the mean value of the critical speed whatever the unbalance. The amplitude at critical speed is more sensitive to bump height manufacturing errors and to unbalance. Its mean value increases with the unbalance and with the magnitude of manufacturing errors (while the critical speed was constant with both unbalance and manufacturing errors). The relative standard deviation of the mean amplitude at critical speed is also more sensitive to manufacturing errors.

These results can explain the differences obtained when testing aerodynamic foil bearings of the same design. Moreover, they can be integrated in a design procedure as requirements for limiting manufacturing errors.

## Nomenclature

$C_r$, design radial clearance, [m]

$C$, damping, [Ns/m]

$E$, Young modulus of elasticity, [Pa]

$e$, foil thickness, [m]

$e_B$, unbalance [g.mm]

$F$, force and force vector, [N]

$f$, friction coefficient

$g$, gap, [m]

$\boldsymbol{G}$, gyroscopic matrix

$h$, film thickness, [m]

$h_b$, bump height, [m]

$I_p$, $I_d I_d$, polar and diametral moment of inertia, [kgm$^2$]

$k$, $K$, stiffness, [N/m]

$\boldsymbol{L}$, matrix, [N/m]

$M$, mass [kg]

$L$, bearing length, [m]

$l_0$, bump half width, [m]

$N$, number of contacts or of samples

$n$, number of iterations

$nb$, number of bumps

$nx$, number of circumf. discretization points

$P$, $\tilde{P}$, pressure, [Pa]

$p$, bump pitch, [m]

$\boldsymbol{q}$, coordinate vector

$R$, bearing radius, [m]

$S$, number of samples

$T$, rotation period, [s]

$t$, $\Delta t$, time and time step, [s]

$u$, displacement, [m]

$W_{x,y}$, static load, [N]

$x$, $y$, z, Cartesian coordinates

$X$, $Y$, axes of the Cartesian coordinates system

$\mu$, dynamic viscosity, [Pa·s]

$\Delta l$, bump spring elongation, [m]

$\delta$, distance from center of mass, [m]

$\varepsilon$, penalty parameter, [N/m]

$\eta$, structural damping coefficient

$\sigma$, standard deviation, [m]

$\bar{\lambda}$, augmented Lagrange multiplier, [N]

$\theta$, $\psi$, angular coordinate, [rad]

$\Pi$, potential energy, [j]

$\nu$, Poisson coefficient

$\Omega$, rotation speed, [rad/s]

*Subscripts*

*ALM*, augmented Lagrange multiplier

*ax*, axially averaged

*b*, bump

*cntct*, contact

*ext*, external ambient

*f*, friction

G, center of gravity

*i, j*, bump number

*n*, normal

*p*, pressure

*r, R*, rotor

*t*, top foil

*0*, initial value

## References

[1] Heshmat, H., Walowit, J. A., and Pinkus, O., 1983, "Analysis of Gas-Lubricated Foil Journal Bearings", ASME J. of Lub. Tech, 105, pp. 647-655.

[2] Chen, M. H., Howarth, R., Geren, B., Theylacker, J.C., Soyars, W.M., 2001, "Application of Foil Bearings to Helium Turbocompressor", Proceedings of the 30th Turbomachinery Symposium, Texas A&M University, Houston, Texas, USA.

[3] Dellacorte, C., DellaCorte, C., and Valco, M. J., 2000, "Load Capacity Estimation of Foil Air Journal Bearings for Oil-Free Turbomachinery Applications", STLE Tribology Transactions, 43(4), pp. 795-801.

[4] Someya, T. (Ed.), 1989, *Journal-Bearing databook*, Springer-Verlag Berlin Heidelberg, p. 326.

[5] Dellacorte, C., Radil, K. Bruckner, R.J., Howard, S.A., 2008, “Design, Fabrication and Performance of Open Source Generation I and II Compliant Hydrodynamic Gas Foil Bearings”, Tribology Transactions, 51, p. 254-264.

[6] Shalash, K., Schiffmann, J., 2017, “On the manufacturing of compliant foil bearings”, J. Manufacturing Processes, 25 : 357-368.

[7] Fatu, A., Arghir, M., 2018, “Numerical Analysis of the Impact of Manufacturing Errors on the Structural Stiffness of Foil Bearings”, ASME J. Eng. Gas Turbines Power, 140(4): 041506.

[8] Fatu, A., Arghir, M., 2018, “Influence of Manufacturing Errors on the Unbalance Response of Aerodynamic Foil Bearings”, Proceedings of the 10th International Conference on Rotor Dynamics – IFToMM.

[9] Heshmat, H., Walowit, J. A., Pinkus, O., 1983, “Analysis of Gas-Lubricated Compliant Thrust Bearings”, J. of Lubrication Tech, 105(4): 638-646.

[10] Rubio, D., San Andres, L., 2007, “Structural Stiffness, Dry Friction Coefficient, and Equivalent Viscous Damping in a Bump-Type Foil Gas Bearing”, J. Eng. Gas Turbines Power, 129(2): 494-502.

[11] Kim, T.H., San Andres, L., 2009, “Effect of Side Feed Pressurization on the Dynamic Performance of Gas Foil Bearings: A Model Anchored to Test Data”, J. Eng. Gas Turbines Power, 131(1): 012501

[12] Kim, D., Park, S., 2009, “Hydrostatic Air Foil Bearings: Analytical and Experimental Investigations”, Tribol. Int. , 42(3): 413-425.

[13] Temis, Y.M., Temis, M.Y., Meshcheryakov, A.B., 2013, “Gas-dynamics Foil Bearing Model”, J. Friction and Wear, 32(3): 212-220.

[14] Zywica G., 2011, “The static performance analysis of the foil bearing structure”, Acta Mechanica et Automatica, 5(4): 119-122.

[15] Le Lez, S., Arghir, M., Frêne, J., 2009, “A Dynamic Model for Dissipative Structures Used in Bump-Type Foil Bearings”, Tribol. Trans., 51(5): 562-572.

[16] Le Lez, S., Arghir, M., Frêne, J., 2007, A New Bump-Type Foil Bearing Structure Analytical Model, ASME J. Eng Gas Turbines Power, 129(4): 1047-1057.

[17] Hoffmann, R., Munz, O., Pronobis, T., Barth, E., Liebich, R., 2016, “A valid method of gas foil bearing parameter estimation: A model anchored on experimental data”, J. Mechanical Engineering Science, 0(0): 1-18.

[18] Von Osmanski, S., Larsen, J.S., Santos, I.F., 2017, “A fully coupled air foil bearing model considering friction – Theory & experiment”, J. of Sound and Vibration, 400: 660-679.

[19] Arghir, M, Benchekroun, O., 2018, “A simplified structural model of bump-type foil bearings based on contact mechanics including gaps and friction”, Tribology International, vol. 134, June 2019, 129-144.

[20] Arghir, M, Benchekroun, O., 2019, A New Structural Bump Foil Model With Application From Start-Up to Full Operating Conditions, J. Eng. Gas Turbines Power. Oct 2019, 141(10): 101017 (12), GTP-19-1332.

[21] Dessombz, O., Diniz, A., Thouverez, F., Jézéquel, L., 1999, “Analysis of Stochastic Structures: Perturbation Method and Projection on Homogeneous Chaos”, Proceedings of SPIE –The International Society for Optical Engineering.

[22] Driot, N., 2002, *Etude de la dispersion vibroacoustique des transmissions par engrenages*, Thèse de doctorat de l'Ecole Centrale de Lyon N° d'ordre 2002-34, 172 p.

[23] Morris, A. S., Langari, R., 2012, *Measurement and Instrumentation: Theory and Application*, Elsevier, Academic Press publications, 617 p.

[24] Harding, B., Tremblay, C., Cousineau, D. 2014, "Standard errors: A review and evaluation of standard error estimators using Monte Carlo simulations", The Quantitative Methods for Psychology, 10(2), pp. 102-123.

[25] Wriggers, P., Zavarise, G., 2006, *Computational Contact Mechanics*, Springer-Verlag Berlin Heidelberg, Second Edition, 518 p.

[26] Frene, J., Nicolas, D., Degueurce, B., Berthe, D., Godet, M., 1990, *Lubrification hydrodynamique. Paliers et Butées*, Editions Eyrolles, 488 p.

[27] Greenwood, J. A., Williamson, J. B. P., 1966, «Contact of Nominally Flat Surfaces» Proc. R. Soc. Lond. A, vol. 295, n° %11442, pp. 300-319.

[28] Benchekroun, O., Arghir, M., 2019, "Impact of bump height manufacturing errors on the unbalance response of a 4dof rigid rotor", SIRM 2019 – 13th International Conference on Dynamics of Rotating Machines, Copenhagen, Denmark, 13th – 15th February.

## List of figures

Figure 1 Bump type foil bearing of first generation

Figure 2: Description of bump foil errors.

Figure 3 : Gaps and degrees of freedom of the structural model

Figure 4 : Discretization of the bump foil with 4DOF per bump

Figure 5: Load versus rotor static displacement

Figure 6: Variation of the structural stiffness with the standard deviation of bump heights

Figure 7: Variation of the loading/unloading dissipated energy with the standard deviation of bump heights

Figure 8: Variation of the standard deviation/mean value with the standard deviation of bump heights

Figure 9: Variation of the standard deviation/mean value with the standard deviation of bump heights in +X and +Y directions (frict. coeff.=0.3)

Figure 10: Circumferential discretization of the top and bump foils

Figure 11 : Dynamic displacements of the 2d.o.f. rotor calculated with different time steps

Figure 12 : Notations and coordinate system for a rigid rotor

Figure 13 : Synchronous amplitudes following X direction of the unbalance response of the 4dof rotor-bearing system.

Figure 14: Synchronous X amplitudes of the foil bearing from the unbalance response of the 4dof rotor-bearing system

Figure 15: Mean value and dimensionless standard deviation of the (first) critical speed of the 4d.o.f. rotor

Figure 16: Mean value and dimensionless standard deviation of the synchronous X amplitudes of the foil bearing at the (first) critical speed

Figure 17: Histograms of the critical speed and of X maximum amplitudes (0,32 gmm unbalance and 1% magnitude of the manufacturing errors)

Figure 18: Mean critical speed and X maximum amplitude vs. the number of samples (0,32 gmm unbalance and 1% magnitude of the manufacturing errors)

## List of tables

Table 1: Geometric and mechanical characteristics of the foil